Adult spiny mice (*Acomys*) exhibit endogenous cardiac recovery in response to myocardial infarction

Hsuan Peng[1*], Kazuhiro Shindo[1*], Renée R. Donahue[1], Erhe Gao[2], Brooke M. Ahern[3], Bryana M. Levitan[3,4], Himi Tripathi[1], David Powell[4], Ahmed Noor[4], Jonathan Satin[3#], Ashley W. Seifert[5#], Ahmed Abdel-Latif[1,4,6#]

[1] *Saha Cardiovascular Research Center, College of Medicine, University of Kentucky*

[2] *The Center for Translational Medicine, Lewis Katz School of Medicine, Temple University, Philadelphia, PA, USA*

[3] *Department of Physiology, College of Medicine, University of Kentucky*

[4] *Gill Heart and Vascular Institute and Division of Cardiovascular Medicine, University of Kentucky*

[5] *Department of Biology, University of Kentucky*

[6] *The Lexington VA Medical Center*

***These authors contributed equally to the study**

[#]To whom correspondence should be addressed: Jonathan Satin: Jonathan.Satin@uky.edu; Ashley W. Seifert: awseifert@uky.edu and Ahmed Abdel-Latif: abdel-latif@uky.edu

Abstract

Complex tissue regeneration is extremely rare among adult mammals. An exception, however, is the superior tissue healing of multiple organs in spiny mice (*Acomys*). While *Acomys* species exhibit the remarkable ability to heal complex tissue with minimal scarring, little is known about their cardiac structure and response to cardiac injury. In this study, we first examined baseline *Acomys* cardiac anatomy and function in comparison with the commonly used laboratory *Mus* strains (C57BL6 and SWR). Our results demonstrated comparable cardiac anatomy and function between *Acomys* and *Mus*, but *Acomys* exhibited a higher percentage of cardiomyocytes exhibiting immature characteristics. In response to myocardial infarction, all animals experienced a comparable level of initial cardiac damage. However, *Acomys* demonstrated superior ischemic tolerance and cytoprotection in response to injury as evidenced by cardiac functional stabilization, higher survival rate and smaller scar size 50 days after injury compared to the inbred and outbred mouse strains. Overall, these findings demonstrate augmented myocardial preservation in spiny mice post-MI and establish *Acomys* as a new adult mammalian model for cardiac research.

Introduction

Significant clinical advances for heart revascularization and next generation medical therapies have improved the mortality rate after myocardial infarction (MI).[1] The initial ischemic insult, even with timely revascularization, is followed by microvascular damage and infarct expansion leading to exacerbated damage.[2] Unfortunately, no therapies exist to limit myocardial damage from MI and the ensuing infarct expansion where millions of recovering patients progress to develop heart failure (HF). This is because the normal healing response to tissue injury in adult mammals is fibrotic repair; an effective short-term strategy, but one that leads to compromised tissue function. Fibrotic repair is the default strategy in the adult heart where it is the leading cause of the clinical HF epidemic.[3] Multiple therapies developed for limiting infarct expansion or cardiac repair based on animal models have achieved only modest clinical success in humans. A failure to translate basic research findings into successful clinical treatments can be traced, in part, to a lack of adult mammalian models possessing the ability of myocardial preservation.

In contrast to humans[4-6], the ability to regenerate injured organs is widespread among vertebrates. Fishes, newts, and salamanders have extensive regenerative ability, and can functionally replace heart tissue after amputation or severe injury by expediting revascularization[7] and by mobilizing a highly proliferative cardiomyocyte pool[8,9]. Specifically, zebrafish are a well-characterized model for adult cardiac regeneration with the documented ability to recover from a plethora of heart injuries including apical resection,[10] cryo-injury,[11] and coronary artery ligation. Neonatal mice are also capable of limiting the initial damage and repairing the myocardium after excision and ischemic injury during the first few days after birth.[12] In contrast, most adult mammals generally exhibit poor regenerative capacity, especially as it pertains to recovering from heart damage. Spiny mice (*Acomys spp.*) are murid rodents found throughout Africa, the Middle East and Western Asia. These rodents exhibit a number of special traits;[13] tantamount among them is the ability to regenerate skin, complex

tissue[14-19] and nephric tissue.[20] At present, how spiny mice respond to heart injury and the extent to which they can recover remains unknown, although a recent review on the topic raised the intriguing possibility that they might exhibit enhanced cardiac healing.[21]

To rigorously examine how spiny mice respond to heart damage, we first detail *Acomys* heart structure and cardiac function in comparison to the most widely used inbred laboratory *Mus* model of cardiac injury (C57BL6). For comparative purposes we also used the Swiss Webster outbred strain (SWR) to account for greater genetic diversity within our spiny mouse population. This cross-species characterization indicates similar cardiac structure and comparable baseline function among spiny mice and the examined mouse strains. We next conducted a comparative analysis of these animals in response to permanent coronary artery ligation (MI). In contrast to the mouse strains studied, *Acomys* showed significantly improved survival and enhanced myocardial preservation following ischemic injury. The ability of *Acomys* to recover from ischemic injury is coincident with greatly improved angiogenesis rarely seen in adult mammals and unique cardiomyocyte characteristics (higher percentage of small, mono-nucleated and diploid CMs, T-type calcium channels). These findings in *Acomys* support a rapid angiogenic response into fibrotic tissue which limits scar spread and enhances ischemic tolerance in response to MI.

87 **Methods**

88 **Detailed methods are described in the Supplementary Methods**

89 **Animal care**

90 Male *Acomys cahirinus* (6-8 months old, sexually mature animals) were obtained from
91 our in-house breeding colony. Male *Mus musculus* (8-12 weeks, sexually mature animals)
92 C57BL6 were obtained from the Jackson Laboratory, Bar Harbor, ME and outbred SWR were
93 obtained from Charles River. Both strains were housed at the University of Kentucky,
94 Lexington, KY. All animal procedures were approved by the University of Kentucky
95 Institutional Animal Care and Use Committee (IACUC #: 2019-3254, 2013-1155 and 2011-
96 0889).

97

98 **Murine model of myocardial infarction**

99 MI surgery was performed using a minimally invasive permanent left anterior
100 descending artery (LAD) ligation model as previously described.[22]

101

102 **Cardiomyocyte isolation and measurements**

103 Ventricular cardiomyocytes were isolated using the Langendorff method as previously
104 described[23] and are further detailed in the supplementary methods. Images used to analyze
105 cardiomyocyte surface area and nucleation were acquired using an Olympus IX-71 and
106 Olympus BX53 microscopes (Olympus, Tokyo, Japan) at 10x magnification. Olympus cellSens
107 software was used to determine cell surface area and number of nuclei. Nuclear volume and
108 ploidy were determined by Imaris reconstruction of z-stack images acquired using a Nikon Ti,
109 A1 confocal microscope (Nikon, Japan) with a step size of 3 μm and 40x oil immersion
110 objective.

111

112 **Echocardiography**

113 Echocardiography was acquired using a Vevo 3100 (VisualSonics, Toronto, Canada)
114 equipped with a MX550D 25-55 MHz linear array transducer. Cardiac function was assessed
115 as previously described.[22] Echocardiographic imaging and analyses were performed by a
116 blinded investigator.
117

118 **Cardiac Magnetic Resonance Imaging**

119 Cardiac magnetic resonance imaging (CMR) was performed on a 7-Tesla ClinScan
120 system (Bruker, Ettlingen, Germany, http://www.bruker.com) equipped with a 4-element
121 phased-array cardiac coil and a gradient system with a maximum strength of 450 mT/m and a
122 maximum slew rate of 4,500 mT/m/s. Studies were performed within 72 hours of MI and at 14
123 days following injury. For late gadolinium-enhanced magnetic resonance imaging, a 0.6
124 mmol/kg bolus of gadolinium-diethylene triamine pentaacetic acid (Gd-DTPA; Gadavist,
125 Bayer Health Care, Whippany, NJ) was injected using the intraperitoneal route.
126

127 **Electrophysiological recordings and calcium transients**

128 $I_{Ca,L}$ was recorded from freshly isolated cardiomyocytes using the whole-cell
129 configuration of the patch clamp technique, and cytosolic Ca^{2+} transients were collected using
130 fura2-AM as previously described.[23]
131

132 **Tissue collection and Processing**

133 Tissue from all species was collected and weighed immediately at sacrifice. The dry
134 lung weight was collected after incubation at 65° C for three days. Hearts were perfused with
135 PBS (VWR International) followed by 4% PFA (VWR International) fixation via cannulation
136 of the ascending aorta. Hearts were post-fixed overnight at 4°C. Hearts were then cut in half
137 along the long axis at the level of the ligation and transferred to 70% ethanol until embedding.

138 Tissues were then paraffin embedded and sectioned at 5um for immunofluorescence and at
139 8um for Masson's Trichrome and Picrosirius Red staining.
140

141 **Histology**

142 Paraffin-embedded heart sections were stained with Masson's Trichrome or
143 Picrosirius Red. Morphometric analyses and image acquisition were performed using a
144 Olympus BX53 microscope (Olympus, Tokyo, Japan) and NIH ImageJ 1.46R software.
145 Quantification of percent fibrosis and scar thickness are detailed in the supplementary methods.
146 Scar collagen fiber quality was examined under 40x magnification. Cellular density in scar
147 tissue was determined by quantifying DAPI+ nuclei in the infarct region at 60x magnification.
148 Infarct size was also quantified three days post-MI from Masson's Trichrome stained slides as
149 the percentage of left ventricle affected. These images were acquired on Zeiss Axioscan slide
150 scanner at 10x magnification. Images were quantified using Nis-Elements software (Nikon).
151

152 **Immunofluorescence**

153 Immunofluorescence assessments were carried out on deparaffinized and rehydrated
154 sections as previously described.[22] Images were taken with a 40x Oil Immersion lens on a
155 Nikon A1 Confocal Microscope in the University of Kentucky Confocal Microscopy facility.
156 Isolectin staining was performed on tissues from day 50 post-MI and was quantified at both
157 the peri-infarct border and the center of the scar and is presented as total capillary density per
158 mm^2. Baseline isolectin measurements were taken at comparable location to the peri-infarct
159 area. A complete list of antibodies is included in the supplemental data.
160

161 **Statistics**

162 Values are expressed as mean ± standard error of mean (SEM). Data were analyzed
163 using a Student's t-test, one-way ANOVA, repeated-measures ANOVA or mixed-effects

ANOVA with Tukey correction to compare data across species as appropriate. Animal numbers are presented as a range based on the number of animals included in each analysis. These numbers are included in the figure legends. All statistical analyses were performed using the Prism 9 software package (GraphPad, La Jolla, CA).

168 **Results**

169 **Heart and coronary tree anatomy are similar among *Acomys* and *Mus* (C57BL6 and**
170 **SWR)**

171 To assess whether interpretable comparisons could be made across species, we first
172 characterized hearts from *Acomys* and the most commonly used laboratory mouse (*Mus*) strain:
173 C57BL6. To control for lifespan differences between species, we used 6 month old, sexually
174 mature *Acomys* and 8-12 week old *Mus* for these studies. In an attempt to control for increased
175 genetic diversity in *Acomys* as well as their larger size, we also included an outbred Swiss
176 Webster strain (SWR – Charles River). As these outbred mice have not been evaluated for
177 myocardial ischemia research, this strain also allowed us to assess whether they shared
178 similarities with the SWR/J strain that is known to exhibit a high percentage of mononuclear
179 cardiomyocytes (CMs) that contribute to enhanced cardiac recovery after ischemic injury.[24]
180 First, we set out to determine whether baseline differences in cardiac gravimetrics exist
181 between *Acomys* and *Mus* (C57BL6 and SWR). We assessed heart weight (HW) and
182 normalized it to body size (body weight [BW] and tibia length [TL]) to account for overall size
183 differences between species (Fig. 1A-D, and Supplementary Table 1). Although *Acomys*
184 demonstrated a higher mean HW compared to C57BL6 (Fig. 1B), normalized to BW, *Acomys*
185 was not significantly different compared to SWR and exhibited only a slighly lower HW/BW
186 compared to C57BL6 (Fig. 1C). SWR mice exhibited a slightly higher HW compared to
187 *Acomys* and C57BL6 when HW was normalized to TL (Fig. 1D). *Acomys* demonstrated heavier
188 wet lung weight compared to *Mus* (C57BL6 and SWR) (Supplementary Fig. 1A), but lower
189 wet and dry lung weight after normalization by BW (Supplementary Fig. 1B, E). Importantly,
190 dry lung weight before normalization by TL and dry and wet lung weight after normalization
191 by TL were not significantly different across species (Supplementary Fig. 1D-F). The complete
192 data is summarized in Supplementary Table 1.

193 Next, we compared cardiac functional parameters between the three strains and
194 observed comparable baseline cardiac function under physiological conditions across species.
195 Importantly, the global cardiac function as presented by left ventricular ejection fraction and
196 fractional shortening were similar between all groups (Fig. 1E-F). Measures of left ventricular
197 cavity diameter were also comparable between species except for SWR-*Mus* showing slightly
198 larger left ventricular end-diastolic diameter and anterior wall thickness compared to *Acomys*
199 (Fig. 1G-J and Supplementary Table 1). We also assessed gross cardiac structure and coronary
200 tree among *Acomys* and *Mus* (C57BL6 and SWR) and found that cardiac structure was not
201 grossly different between the species upon visual comparison of whole hearts along the short-
202 or long-axis (Supplementary Fig. 1G). Using corrosion casting and intra-aortic infusion of
203 Batson's 17 polymer mixture, we delineated the left coronary anatomy in all three strains.
204 Relevant to permanent coronary ligation, all three animals demonstrated similar course of the
205 left anterior descending artery (LAD) supplying the anterior wall, and of the left circumflex
206 artery supplying the lateral aspect of the left ventricle (Fig. 1K). Coronary blood vessels adopt
207 a hierarchal structure and vascular density leads to enhanced blood supply, angiogenesis and
208 ischemic resistance.[25,26] Thus, we analyzed the bifurcation points of the coronary tree as it
209 supplies the anterior wall of the left ventricle. These analyses showed a similar density of
210 branching points per major artery across species (Fig. 1L). Finally, we assessed capillary
211 density at the mid left ventricular level between species and observed slightly higher capillary
212 density in *Acomys* and SWR-*Mus* compared to C57BL6-*Mus* (Supplementary Fig. 2). These
213 data demonstrate that cardiac anatomy and physiology are comparable between spiny mice and
214 the two inbred laboratory mouse strains C57BL6 and SWR.

215

216 **Adult *Acomys* exhibit a high percentage of cardiomyocytes possessing fetal characteristics**

217 Ventricular cardiomyocyte (CM) phenotype varies across species and chronological

218 age where it can influence the cardiac response to injury.[12,24] In mammals, the presence of
219 mononuclear diploid CMs are indicative of a 'young' heart phenotype that is rarely seen in
220 adult mice.[27, 28] To examine CM phenotype between species, we isolated ventricular CMs from
221 *Mus* and *Acomys* and examined their size, number of nuclei/CM, nuclear characteristics and
222 ploidy. Similar to a prior report,[29] *Acomys* CMs were significantly smaller than C57BL6 and
223 were approximately four times more likely to be mononucleated (*Acomys*: 25.9±5.1% vs.
224 C57BL6: 6.3±2.8%, $P < 0.001$; Fig. 2A-C). Similarly, CM nuclei in *Acomys* were smaller in
225 size (Fig. 2D).[30] We then assessed the ploidy of ventricular CMs across species using 3-
226 dimensional confocal microscopy[31] and found a significantly higher percentage of diploid CMs
227 in *Acomys* with a corresponding lower percentage of >4N CMs (Fig. 2E). Interestingly, SWR-
228 *Mus* CMs were intermediate between *Acomys* and C57BL6 with smaller size and higher
229 percentage of mononuclear CMs as shown for the inbred strain SWR/J in a previous study.[24]

230 The relatively small cell size and higher mononucleation we observed in *Acomys* CMs
231 suggested a higher percentage of CMs exhibiting immature or fetal characteristics. T-tubule
232 organization is highly regular in mature mouse CMs.[32] To assess T-tubule organization we
233 stained CMs with di-8-ANEPPS (Fig. 3A) and evaluated transverse and axial density along
234 with T-tubule spacing. *Acomys* showed significantly reduced transverse and long element
235 densities (Fig. 3B and 3C) without a change in resting T-tubule spacing (Fig. 3D). To further
236 explore the physiological implications of these findings, we conducted electrophysiological
237 studies on isolated ventricular CMs from C57BL6-*Mus* and *Acomys*. In mammalian hearts, the
238 expression of low-voltage activated (T-type calcium channels) is an index of the fetal gene
239 program;[33] therefore, we recorded voltage-dependent I_{Ca} from *Acomys* and *Mus* ventricular
240 myocytes. From a V_{hold} -80mV, a V_{test} step to -25mV elicited little if any discernable current in
241 *Mus* (C57BL6) whereas, at V_{test} -25mV, *Acomys* cardiomyocytes exhibited a transient 'T-type'
242 calcium current ($I_{Ca,T}$) (Fig. 3E, upper panel). Longer lasting calcium current ($I_{Ca,L}$) was

243 prominent with larger depolarizations in *Mus* (C57BL6) and *Acomys* (Fig. 3E, lower panel).
244 The current-voltage relationship showed a prominent $I_{Ca,T}$ component with a peak current
245 between V_{test} -20 and -25mV in *Acomys*, but not in *Mus* (C57BL6) (Fig. 3E).

246 To further dissect $I_{Ca,T}$ from $I_{Ca,L}$, we performed current-voltage curve protocols from
247 V_{hold} -50mV to voltage-inactivate the $I_{Ca,T}$ component (Fig. 3F). Current-voltage relationships
248 for $I_{Ca,T}$-expressing *Acomys* cells showed the prominent $I_{Ca,T}$ appearing as a low-voltage
249 activated current for V_{hold} -80mV but not from V_{hold} –50 mV (Fig. 3F, left). 33% of *Acomys*
250 ventricular cardiomyocytes showed no $I_{Ca,T}$ (Fig 3F, center) but there was no observed
251 correlation of cell size to presence of $I_{Ca,T}$ (Fig. 3F, right). Cell capacitance was significantly
252 lower in *Acomys* compared to *Mus* (C57BL6) (Fig. 3G), consistent with our morphometric
253 analysis (Fig. 2B). Additionally, maximal conductance density trended greater in *Mus*
254 (C57BL6) than *Acomys* (Fig. 3H). Voltage-dependent activation and inactivation of $I_{Ca,L}$ was
255 significantly shifted positive for *Acomys* compared to *Mus* (C57BL6) (Fig. 3I-J).

256 We next explored cytosolic calcium handling. Cytosolic Ca^{2+} transients (CaT) had a
257 larger amplitude (Fig. 3K, left), faster upstroke (Fig. 3K, middle), and more rapid decay (Fig.
258 3K, right) in *Mus* (C57BL6) compared to that observed in *Acomys*. As with CM morphometrics
259 (Fig. 3A-D) and the prevalent expression of a T-type calcium current (Fig. 3E-F) the smaller,
260 slower CaT segregated with a less mature CM phenotype. Immature ventricular CMs also tend
261 to show reduced β-adrenergic receptor (β-AR) acute responsiveness.[34] Therefore, we tested the
262 effect of isoproterenol challenge (ISO). To assess acute ISO responsiveness, we compared
263 within cell before – after ISO. *Mus* (C57BL6) showed increased amplitude and more rapid
264 kinetics (Fig. 3L). By contrast, *Acomys* CaT amplitude and upstroke velocity were not
265 significantly different (P>0.05). Ca^{2+} re-uptake was accelerated by ISO in *Mus* but not in
266 *Acomys* (Fig. 3L, right). Taken together, these data are consistent with an *Acomys*
267 cardiomyocyte phenotype distinct from that of C57BL6-*Mus*. Moreover, these data
268 demonstrate that a high percentage of *Acomys* CMs exhibit characteristics usually associated

269 with *Mus* fetal CMs.

270 ***Acomys* hearts demonstrate enhanced cardiac preservation after ischemic injury**

271 *Acomys* can regenerate complex tissue wounds, but the response to myocardial
272 ischemic (MI) injury remains untested. We next sought to compare the cardiac injury response
273 between *Acomys* and the two strains of *Mus* using the permanent LAD-ligation model of
274 myocardial infarction.[35-37] After injury, all groups showed a comparable drop in cardiac
275 function, reflecting similar injury response as assessed by serial echocardiography (Fig. 4,
276 Supplementary Fig. 3 and Supplementary Table 1). Indeed, there was no significant difference
277 in most of cardiac fucntional parameters at 48 hours after MI (Fig. 4B-F, $P>0.05$). When we
278 assessed the extent of cardiac tissue injury in a subset of animals three days after MI using
279 Mason Trichrome staining, we observed comparable percent infarct between species
280 (Supplementary Fig. 3A). Furthermore, our cardiac MRI imaging showed comparable injury
281 and involvement of the distal anterior wall and apex three days after MI beween species as
282 demonstrated by similar area of late gadolinium enhancement (Supplementary Fig. 4).
283 Interestingly, we observed stabilization in cardiac function and remodeling pararmeters in
284 *Acomys* compared to the progressive deterioration seen in *Mus* strains (C57BL6 and SWR) up
285 to 50 days after injury (Fig. 4B-F). In these analyses, we utilized the delta change from baseline
286 to account for any differences in baseline function between species which allowed us to isolate
287 the analyses to the changes occurring after MI. We observed consistent changes in left
288 ventricular global ejection fraction, as well as measures of left ventricular adverse remodeling
289 such as end-systolic and end-diastolic diameters and volumes (Fig. 4A-F and Supplementary
290 Fig. 3B-F). The enhanced cardiac preservation and reduced adverse cardiac remodeling in
291 *Acomys* was reflected by lower heart/body weight ratio throughout the follow-up period
292 extending to 50 days after MI (Fig. 4G), as well as the aforementioned echocardiographic
293 evidence of smaller ventricular diameters. We also observed significantly lower wet-dry lung
294 weight in *Acomys* compared to *Mus* which is a measure of pulmonary edema and heart failure

295 (Fig. 4H). Importantly, enhanced myocardial preservation in *Acomys* compared to *Mus* was
296 associated with a significant survival advantage (Fig. 4I). As seen in prior reports, the majority
297 of mortality across all species was observed in the first week after MI. However, of those
298 animals that died, while we observed cardiac rupture in 17 C57BL6, we observed none in
299 *Acomys* as visualized in post-mortem necropsies.

300 CMR studies demonstrated reduced scar progression between day 3 (D3) and D14 in
301 *Acomys* compared to the continued infarct expansion seen in *Mus* (Fig. 4J). Our long-term
302 follow-up studies reflected significantly smaller infarct size in *Acomys* compared to *Mus*
303 (C57BL6 and SWR) when assessed using Masson's Trichrome staining 50 days after MI (Fig.
304 5A). We also saw similar results in our studies quantifying the degree of fibrosis using
305 Picrosirius red staining at 50 days after MI (Supplementary Fig. 3G). Furthermore, the resultant
306 scar in *Acomys* appeared thicker with higher cellular density (Fig. 5C), a finding that could
307 potentially explain the lower rupture and mortality rates. To further explore the fibrous tissue
308 alignment of the thicker scar in *Acomys*, we stained cardiac tissue using Picrosirius Red. While
309 the fiber alignment in the *Mus* strains was typical of a scar with highly parallel and compressed
310 collagen bundles, fiber organization in the center of the *Acomys* scar was more porous with less
311 compression (Fig. 5B). Furthermore, our serial scar analysis at days 7, 17 and 50 after MI
312 demonstrated a unique evolution in infarct size between *Mus* and *Acomys* which corroborated
313 the CMR studies (Fig. 6A-D). In contrast to previous reports,[24] our studies showed limited
314 recovery of cardiac functional parameters after MI in SWR-*Mus* (Fig. 4B-F). Taken together,
315 our results demonstrate that *Acomys* exhibit ischemic tolerance and enhanced myocardial
316 preservation after ischemic injury compared to the inbred C57BL6- and outbred SWR-*Mus*
317 strains, respectively.

318

319 ***Acomys* exhibit rapid and enhanced vascularization of the infarct region after ischemic**

injury.

Blood vessel formation following ischemic injury is essential for functional stabilization. Following ischemic injury, vascular damage ensues in the area surrounding the original infarct region and leads to infarct expansion, development of adverse cardiac remodeling and heart failure.[2,38-40] Several studies have shown successful reduction of infarct expansion through effective angiogenesis and vascular maturation.[41,42] We assessed the vascular density in the peri-infarct region in *Acomys* and *Mus* strains and observed an increased density of capillaries (isolectin+ cells) in *Acomys* compared to C57BL6-*Mus* (Fig. 7A). As commonly observed in adult mammals following MI, both *Mus* strains exhibited reduced vascular density in the scar center; by contrast, *Acomys* showed enhanced vascular density extending into the scar center (Fig. 7A). Additionally, enhanced angiogenesis was linked to more proliferating endothelial cells (isolectin+/EdU+) in the peri-infarct region and scar center in *Acomys* compared to both *Mus* strains (Fig. 7B). In support of enhanced angiogenesis, we observed a significantly higher density of mature blood vessels (α-SMA+) in the peri-infarct region in *Acomys* while the presence of these mature vessels was negligible in *Mus* strains (Fig. 7C). Taken together, in response to MI our data support rapid and enhanced angiogenesis followed by vascular maturation in *Acomys* compared to *Mus*. This can explain, at least in part, the ischemic tolerance, reduced infarct expansion and the thicker, cellularly dense scar in *Acomys* compared to *Mus*.

339 **Discussion**

340 Spiny mice (*Acomys*) represent a novel mammalian model to explore endogenous
341 cardiac repair consistent with their enhanced regenerative ability for a number of tissues and
342 organs. In this study, we established the anatomical, functional, and cellular characteristics pre-
343 and post-MI in *Acomys* compared to the inbred laboratory mouse strain C57BL6 and the
344 outbred SWR strain. Our results demonstrated comparable cardiac structure, coronary anatomy
345 and functional parameters between the three animals allowing us to appropriately use these
346 animal models for comparative heart injury studies. Interestingly, when comparing
347 cardiomyocytes across species we found that adult *Acomys* possessed a distinct CM phenotype
348 that included features usually observed in immature or fetal *Mus* CMs such as small size,
349 mononucleation and reduced t-tubule density and organization. After ischemic injury, *Acomys*
350 exhibited enhanced ischemic tolerance and significant myocardial preservation, resulting in
351 reduced adverse cardiac remodeling, smaller scar size and, importantly, better survival. Overall,
352 our data supports that *Acomys* show resistance to the type of cardiac damage that compromises
353 other adult mammals, including humans and supports future cardiac studies using this model.

354 Similar to other highly regenerative vertebrates, *Acomys* has emerged as a bona fide
355 mammalian regeneration model for their ability to naturally regrow complex tissues following
356 full-thickness skin injury[14-19] and excision of musculoskeletal tissue from the ear pinna.[16,18,43]
357 In each type of injury, adult *Acomys* were capable of restoring functional tissues, a phenotype
358 that has not been observed in other adult rodents. Our gross anatomical studies established a
359 similar coronary anatomy across species [44] and we found that *Acomys* hearts were similar
360 structurally and anatomically to *Mus*. Importantly, *in vivo* cardiac functional parameters were
361 comparable between the three groups. These findings provided the appropriate foundation for
362 the current study and lay the groundwork for follow-up studies that can inform new therapeutic
363 strategies for ischemic heart disease.

364 Increased mortality and incidence of heart failure following myocardial infarction

365 remains prevalent in modern medicine. While advanced revascularization therapies and
366 mechanical support have slightly improved survival in patients with myocardial infarction,
367 millions develop progressive heart failure every year. Remarkably, *Acomys* exhibited
368 significantly lower mortality after MI compared to both *Mus* strains and this reduction in
369 mortality was related to a reduced incidence of cardiac rupture among *Acomys*. In fact, our
370 histological assessment combined with cardiac MRI studies indicated significant differences in
371 infarct expansion and scar evolution between species. While *Mus* demonstrated progressive
372 infarct expansion, associated with thinning of the anterior wall, *Acomys* showed minimal
373 expansion despite starting with comparable area of injury. These differences in infarct
374 expansion led to favorable cardiac remodeling and functional preservation demonstrated in our
375 echocardiography studies.

376 This unique phenomenon was associated with a rapid angiogenic response that
377 eventually led to superior ischemic tolerance. *Acomys* scars appeared to be more cellularized
378 and had higher capillary and mature vessel density compared to *Mus*. This could explain the
379 dramatically lower cardiac rupture rate and enhanced survival we observed in *Acomys*
380 including the stabilization of cardiac function in *Acomys* during long-term follow-up.
381 Preclinical and human MI studies have linked enhanced angiogenesis and vessel maturation
382 with lower rates of infarct expansion.[42,45] Our studies demonstrated superior endothelial cell
383 proliferation and vessel maturation in *Acomys* compared to *Mus* strains which likely accounted
384 for some of the protection seen in our studies.

385 The mammalian heart loses its reparative capability after the first week of life where
386 heart damage results in permanent loss of myocardium combined with fibrotic scarring and
387 adverse remodeling.[12] The transition to fibrotic repair is closely linked with the loss of CM
388 proliferation as CMs enter cell cycle arrest and become mononuclear polyploid or
389 multinucleated.[12,46] However, in other vertebrate species where CMs maintain the lifelong
390 ability to proliferate (e.g., zebrafish and newts), cardiac regeneration is still possible.[46, 47] One

391 of the hallmarks of regenerative hearts is the relatively high frequency of mononucleated
392 diploid CMs.[46-48] This evidence suggests that higher proportions of mononuclear diploid
393 CMs are associated with higher regenerative potential following ischemic injury.[24]
394 Interestingly, our results showed that outbred SWR-*Mus* possessed an intermediate CM
395 phenotype between *Acomys* and C57BL6 with respect to CM size and nuclei number. Despite
396 possessing this CM phenotype, outbred SWR had nearly the same mortality as C57BL6
397 suggesting that rapid angiogenesis may be a key component to facilitate the protective features
398 conferred by having a larger population of smaller, mononucleate CMs. In fact, cardiac tissue
399 requires vascularization for supporting the high metabolic activity of CMs,[49] and our current
400 findings support rapid angiogenic invasion into new fibrotic tissue as a mechanism to resist
401 cardiac damage. Future studies are necessary to explore CM behavior across species and how
402 this may relate to enhanced angiogenesis.

403 There are two types of Ca^{2+} channels in cardiomyocytes, L-type and T-type. L-type
404 Ca^{2+} channels are highly expressed in the adult heart and are important therapeutic targets for
405 the management of various cardiovascular diseases. In contrast, T-type Ca^{2+} channels are rarely
406 found in adults and are present in fetal and early postnatal mice.[50] In our cell electrophysiology
407 studies, *Acomys* exhibited a higher percentage of T-type Ca^{2+} channels. This feature is
408 consistent with a higher prevalence of phenotypically 'young' CMs in *Acomys* compared to
409 *Mus* (C57BL6). Furthermore, immature ventricular cardiomyocytes in *Mus* showed reduced
410 Ca^{2+} transient amplitude, slower kinetics,[51] and attenuated β-adrenergic receptor
411 responsiveness.[52] While this unique phenomena in *Acomys* was associated with superior
412 myocardial preservation after ischemic injury, because we did not examine Ca^{2+} channels in
413 outbred SWR mice, we do not know if this feature is associated with the prevalence of small,
414 diploid, mononucleated CMs. However, it is interesting to note that although our CM
415 characterization studies showed that outbred SWR possessed a higher prevalence of small,
416 diploid, mononucleated CMs, this feature alone did not confer the type of enhanced myocardial

observed in previous work using inbred SWR/J mice.[24] This would suggest a synergy between CM phenotype and enhanced angiogenesis with respect to cardiac preservation following MI. Future studies are necessary to examine the proliferative potential of adult CMs in *Acomys* and *Mus* as well as their potential to adequately respond to myocardial injury.

In conclusion, our study presents *Acomys* as a novel model for cardiac research with comparable cardiac structure, function and anatomy to C57BL6- and SWR-*Mus*. *Acomys* exhibited a distinct cardiomyocyte phenotype and angiogenic response resulting in enhanced recovery and ischemic tolerance after ischemic injury. It is important to note that while we do not see clear evidence of cardiac regeneration, the enhanced myocardial preservation seen in *Acomys* could uncover important therapeutic targets for millions of patients who develop ischemic cardiomyopathy after myocardial infarction. Future studies will focus on the mechanism and potential for these phenotypic differences to foster myocardial preservation and repair instead of scarring and heart failure in models of cardiac disease.

Acknowledgments: The authors would like to thank Josh Sarli for his help with *Acomys* husbandry and Thomas Wilkop Ph.D at the microscopy core at the University of Kentucky for his assistance with imaging. We thank the Markey Cancer Center and the COBRE histology core for their assistance with the tissue specimen preparation. We thank Binoy Joseph for his assistance in imaging and the Spinal Cord and Brain Injury Research Center for use of their imaging equipment. We thank Beverly Meacham and the University of Kentucky MRISC center for the assistance with cardiac MRI studies.

JS, AWS, AAL, KS, HP, RRD designed the project and experiments. KS, HP, RRD, EG, BMA, BML, DP, HT, and AN performed all the experiments.

KS, HP, RRD, BMA, BML, JS, AAL analyzed the data and KS, HP, JS, AWS, AAL wrote the manuscript. All authors commented on and edited the final version.

Funding: Dr. Abdel-Latif is supported by NIH Grant R01 HL124266. Work in Dr. Seifert's lab is supported by NIH R01 AR070313. The content in this article is solely the responsibility of the authors and does not necessarily represent the official views of the National Institutes of Health.

Markey Cancer Center Core: This research was supported by the Biospecimen Procurement and Translational Pathology Shared Resource Facility of the University of Kentucky Markey Cancer Center (P30CA177558)

COBRE Core: Research reported in this publication was supported by an Institutional Development Award (IDeA) from the National Institute of General Medical Sciences of the National Institutes of Health under grant number P30 GM127211.

Competing Interests: The authors declare that there are no competing interests.

Data Availability: The authors declare that all the data supporting the findings of this study are available within the paper and are contained within supplementary information.

460 **References.**

461 1. Benjamin, E.J., *et al.* Heart Disease and Stroke Statistics-2017 Update: A Report From the
462 American Heart Association. *Circulation* **135**, e146-e603 (2017).
463 2. Iwakura, K. Modulation of individual susceptibility to the no-reflow phenomenon after
464 acute myocardial infarction. *Curr Pharm Des* **19**, 4519-4528 (2013).
465 3. McAloon, C.J., *et al.* The changing face of cardiovascular disease 2000-2012: An analysis
466 of the world health organisation global health estimates data. *Int J Cardiol* **224**, 256-264
467 (2016).
468 4. Pfeffer, M.A. & Braunwald, E. Ventricular remodeling after myocardial infarction.
469 Experimental observations and clinical implications. *Circulation* **81**, 1161-1172 (1990).
470 5. Jugdutt, B.I. Ventricular remodeling after infarction and the extracellular collagen matrix:
471 when is enough enough? *Circulation* **108**, 1395-1403 (2003).
472 6. Struthers, A.D. Pathophysiology of heart failure following myocardial infarction. *Heart* **91**
473 **Suppl 2**, ii14-16; discussion ii31, ii43-18 (2005).
474 7. Marin-Juez, R., *et al.* Coronary Revascularization During Heart Regeneration Is Regulated
475 by Epicardial and Endocardial Cues and Forms a Scaffold for Cardiomyocyte Repopulation.
476 *Dev Cell* **51**, 503-515 e504 (2019).
477 8. Bader, D. & Oberpriller, J.O. Repair and reorganization of minced cardiac muscle in the
478 adult newt (Notophthalmus viridescens). *J Morphol* **155**, 349-357 (1978).
479 9. Flink, I.L. Cell cycle reentry of ventricular and atrial cardiomyocytes and cells within the
480 epicardium following amputation of the ventricular apex in the axolotl, Amblystoma
481 mexicanum: confocal microscopic immunofluorescent image analysis of
482 bromodeoxyuridine-labeled nuclei. *Anat Embryol (Berl)* **205**, 235-244 (2002).
483 10. Poss, K.D., Wilson, L.G. & Keating, M.T. Heart regeneration in zebrafish. *Science* **298**,
484 2188-2190 (2002).
485 11. Honkoop, H., *et al.* Single-cell analysis uncovers that metabolic reprogramming by ErbB2
486 signaling is essential for cardiomyocyte proliferation in the regenerating heart. *Elife*
487 **8**(2019).
488 12. Porrello, E.R., *et al.* Transient regenerative potential of the neonatal mouse heart. *Science*
489 **331**, 1078-1080 (2011).
490 13. Haughton, C.L., Gawriluk, T.R. & Seifert, A.W. The Biology and Husbandry of the African
491 Spiny Mouse (Acomys cahirinus) and the Research Uses of a Laboratory Colony. *J Am*
492 *Assoc Lab Anim Sci* **55**, 9-17 (2016).
493 14. Harn, H.I., *et al.* Symmetry breaking of tissue mechanics in wound induced hair follicle
494 regeneration of laboratory and spiny mice. *Nat Commun* **12**, 2595 (2021).
495 15. Brant, J.O., Yoon, J.H., Polvadore, T., Barbazuk, W.B. & Maden, M. Cellular events during
496 scar-free skin regeneration in the spiny mouse, Acomys. *Wound Repair Regen* **24**, 75-88
497 (2016).

498 16. Gawriluk, T.R., *et al.* Comparative analysis of ear-hole closure identifies epimorphic
499 regeneration as a discrete trait in mammals. *Nat Commun* **7**, 11164 (2016).
500 17. Jiang, T.X., Harn, H.I., Ou, K.L., Lei, M. & Chuong, C.M. Comparative regenerative
501 biology of spiny (Acomys cahirinus) and laboratory (Mus musculus) mouse skin. *Exp*
502 *Dermatol* **28**, 442-449 (2019).
503 18. Matias Santos, D., *et al.* Ear wound regeneration in the African spiny mouse Acomys
504 cahirinus. *Regeneration (Oxf)* **3**, 52-61 (2016).
505 19. Seifert, A.W., *et al.* Skin shedding and tissue regeneration in African spiny mice (Acomys).
506 *Nature* **489**, 561-565 (2012).
507 20. Okamura, D.M., *et al.* Scarless repair of acute and chronic kidney injury in African Spiny
508 mice (Acomys cahirinus). *bioRxiv* **315069.**(2018).
509 21. Maden, M. & Varholick, J.A. Model systems for regeneration: the spiny mouse, Acomys
510 cahirinus. *Development* **147**(2020).
511 22. Al-Darraji, A., *et al.* Azithromycin therapy reduces cardiac inflammation and mitigates
512 adverse cardiac remodeling after myocardial infarction: Potential therapeutic targets in
513 ischemic heart disease. *PLoS One* **13**, e0200474 (2018).
514 23. Ahern, B.M., *et al.* Myocardial-restricted ablation of the GTPase RAD results in a pro-
515 adaptive heart response in mice. *J Biol Chem* **294**, 10913-10927 (2019).
516 24. Patterson, M., *et al.* Frequency of mononuclear diploid cardiomyocytes underlies natural
517 variation in heart regeneration. *Nat Genet* **49**, 1346-1353 (2017).
518 25. Carmeliet, P. & Jain, R.K. Molecular mechanisms and clinical applications of angiogenesis.
519 *Nature* **473**, 298-307 (2011).
520 26. Potente, M., Gerhardt, H. & Carmeliet, P. Basic and therapeutic aspects of angiogenesis.
521 *Cell* **146**, 873-887 (2011).
522 27. Alkass, K., *et al.* No Evidence for Cardiomyocyte Number Expansion in Preadolescent
523 Mice. *Cell* **163**, 1026-1036 (2015).
524 28. Soonpaa, M.H., Kim, K.K., Pajak, L., Franklin, M. & Field, L.J. Cardiomyocyte DNA
525 synthesis and binucleation during murine development. *Am J Physiol* **271**, H2183-2189
526 (1996).
527 29. Hirose, K., *et al.* Evidence for hormonal control of heart regenerative capacity during
528 endothermy acquisition. *Science* **364**, 184-188 (2019).
529 30. Lozoya, O.A., Gilchrist, C.L. & Guilak, F. Universally Conserved Relationships between
530 Nuclear Shape and Cytoplasmic Mechanical Properties in Human Stem Cells. *Sci Rep* **6**,
531 23047 (2016).
532 31. Broughton, K.M., *et al.* Cardiac interstitial tetraploid cells can escape replicative
533 senescence in rodents but not large mammals. *Commun Biol* **2**, 205 (2019).
534 32. Sipido, K.R., Carmeliet, E. & Van de Werf, F. T-type Ca2+ current as a trigger for Ca2+
535 release from the sarcoplasmic reticulum in guinea-pig ventricular myocytes. *J Physiol* **508**

536 **(Pt 2)**, 439-451 (1998).
537 33. Nuss, H.B. & Houser, S.R. T-type Ca2+ current is expressed in hypertrophied adult feline
538 left ventricular myocytes. *Circ Res* **73**, 777-782 (1993).
539 34. Schroder, E., Byse, M. & Satin, J. L-type calcium channel C terminus autoregulates
540 transcription. *Circ Res* **104**, 1373-1381 (2009).
541 35. Dick, S.A., *et al.* Self-renewing resident cardiac macrophages limit adverse remodeling
542 following myocardial infarction. *Nat Immunol* **20**, 29-39 (2019).
543 36. Epelman, S., Liu, P.P. & Mann, D.L. Role of innate and adaptive immune mechanisms in
544 cardiac injury and repair. *Nat Rev Immunol* **15**, 117-129 (2015).
545 37. Lindsey, M.L., *et al.* Guidelines for experimental models of myocardial ischemia and
546 infarction. *Am J Physiol Heart Circ Physiol* **314**, H812-H838 (2018).
547 38. Heusch, G. The Coronary Circulation as a Target of Cardioprotection. *Circ Res* **118**, 1643-
548 1658 (2016).
549 39. Wang, J., Toan, S. & Zhou, H. Mitochondrial quality control in cardiac microvascular
550 ischemia-reperfusion injury: New insights into the mechanisms and therapeutic potentials.
551 *Pharmacol Res* **156**, 104771 (2020).
552 40. Kloner, R.A. No-reflow phenomenon: maintaining vascular integrity. *J Cardiovasc*
553 *Pharmacol Ther* **16**, 244-250 (2011).
554 41. Nazir, S.A., *et al.* Strategies to attenuate micro-vascular obstruction during P-PCI: the
555 randomized reperfusion facilitated by local adjunctive therapy in ST-elevation myocardial
556 infarction trial. *Eur Heart J* **37**, 1910-1919 (2016).
557 42. Zhang, S., *et al.* Comparison of various niches for endothelial progenitor cell therapy on
558 ischemic myocardial repair: coexistence of host collateralization and Akt-mediated
559 angiogenesis produces a superior microenvironment. *Arterioscler Thromb Vasc Biol* **32**,
560 910-923 (2012).
561 43. Simkin, J., Gawriluk, T.R., Gensel, J.C. & Seifert, A.W. Macrophages are necessary for
562 epimorphic regeneration in African spiny mice. *Elife* **6**(2017).
563 44. Ostadal, B., Schiebler, T.H. & Rychter, Z. Relations between development of the capillary
564 wall and myoarchitecture of the rat heart. *Adv Exp Med Biol* **53**, 375-388 (1975).
565 45. Fitzpatrick, J.R., 3rd, *et al.* Tissue-engineered pro-angiogenic fibroblast scaffold improves
566 myocardial perfusion and function and limits ventricular remodeling after infarction. *J*
567 *Thorac Cardiovasc Surg* **140**, 667-676 (2010).
568 46. Kikuchi, K., *et al.* Primary contribution to zebrafish heart regeneration by gata4(+)
569 cardiomyocytes. *Nature* **464**, 601-605 (2010).
570 47. Oberpriller, J.O. & Oberpriller, J.C. Response of the adult newt ventricle to injury. *J Exp*
571 *Zool* **187**, 249-253 (1974).
572 48. Jopling, C., *et al.* Zebrafish heart regeneration occurs by cardiomyocyte dedifferentiation
573 and proliferation. *Nature* **464**, 606-609 (2010).

574 49. Chiu, L.L., Radisic, M. & Vunjak-Novakovic, G. Bioactive scaffolds for engineering
575 vascularized cardiac tissues. *Macromol Biosci* **10**, 1286-1301 (2010).
576 50. Cribbs, L.L.*, et al.* Identification of the t-type calcium channel (Ca(v)3.1d) in developing
577 mouse heart. *Circ Res* **88**, 403-407 (2001).
578 51. Balaguru, D.*, et al.* Role of the sarcoplasmic reticulum in contraction and relaxation of
579 immature rabbit ventricular myocytes. *J Mol Cell Cardiol* **29**, 2747-2757 (1997).
580 52. Kuznetsov, V., Pak, E., Robinson, R.B. & Steinberg, S.F. Beta 2-adrenergic receptor actions
581 in neonatal and adult rat ventricular myocytes. *Circ Res* **76**, 40-52 (1995).
582

583 **Figure legends.**

584 **Figure 1. Characteristics of *Acomys* heart physiology and anatomy at baseline.**

585 (A-J) Measures of body weight (BW) and heart weight in *Mus*-C57BL6 (N = 10), *Mus*-SWR
586 (N = 19) and *Acomys* (N = 22). Analyses demonstrate comparable heart weight across species
587 when normalized by body weight (BW) and tibia length (TL) (values are means ± S.E.M, *P
588 < 0.05, **P<0.01, and ***P<0.001 by one-way ANOVA and Dunnett correction with *Acomys*
589 as control). Ejection fraction (F=4.1, *P<0.05) (E), fractional shortening (F=0.96, P>0.05) (F),
590 left ventricular end-diastolic diameter (LVEDD) (F=14.8, **P<0.01) (G), left ventricular end-
591 systolic diameter (LVESD) (F=4.6) (H), left ventricular anterior wall (LVAW) (F=14.9,
592 *P<0.05) (I), left ventricular posterior wall (LVPW) (F=6.4) (J) (N = 30 C57BL6-*Mus*, 10
593 SWR-*Mus* and 10 *Acomys*). (K) Representative images showing comparable left anterior
594 descending artery coronary anatomy across species using intra-aortic infusion of Batson's 17
595 polymer mixture and corrosion casting (N = 5 each group, scale bar =1 mm). (L) Quantification
596 of coronary branching points of the arterial supply of the left ventricle across species. This
597 analysis shows comparable number of branching points across species with numerically higher
598 (but not statistically significant) branching points in C57BL6-*Mus* and *Acomys* compared to
599 SWR-*Mus*. Detailed statistical output for Figure 1 can be found in the Supplementary
600 Information.

601

602 **Figure 2. *Acomys* cardiomyocytes exhibit features associated with *Mus* immature**
603 **cardiomyocytes.**

604 (A) Representative images of single-cell ventricular suspension stained with DAPI (blue),
605 identifying small, mononuclear and binucleated cardiomyocytes in *Acomys* and larger
606 binucleated cardiomyocytes in *Mus*-C57BL6 with SWR cardiomyocytes being intermediate in
607 size between C57BL6 and *Acomys* (scale bar = 50 μm) with mononuclear and binucleated
608 cardiomyocytes. (B) Quantitative analyses of cell surface area of *Mus*-C57BL6 and *Acomys* (n

609 = 80 to 120 randomly selected CMs/animal and N = 4 each for *Mus*-C57BL6, *Mus*-SWR and
610 *Acomys*, ***$P < 0.001$ by one-way ANOVA; values are means ± S.E.M). (C) Percentage of
611 mono-, bi- and poly-nuclear cardiomyocytes in C57BL6-, SWR-*Mus* and *Acomys* (n = 80 to
612 120 randomly selected CMs/animal, N = 4 mice for each group, values are means ± S.E.M,
613 **$P<0.01$, ***$P < 0.001$ by One-way ANOVA and Dunnet post-hoc analysis, compared to
614 C57BL6-*Mus*). (D) Nuclear volume among isolated cardiomyocytes showing small nuclear
615 volume in SWR-*Mus* and *Acomys* compared to C57BL6-*Mus* (n = 80 to 120 randomly selected
616 CMs/animal, N = 4 mice per group, values are means ± S.E.M, ***$P < 0.001$ by One-way
617 ANOVA and Dunnet's post-hoc analysis, compared to C57BL6-*Mus*). (E) Violin plots, on left,
618 demonstrating the distribution of DAPI fluorescence intensity in cardiomyocyte nuclei as
619 assessed using Imaris on 3D (Z-stack) microscopy images. The right panel shows the
620 percentage of CMs within each ploidy category from the total pool of CMs from each species
621 (2N, 4N, and > 4N) (n = 25 to 35 randomly selected CMs/animal, N = 3 mice for each group).
622

623 **Figure 3. Physiological characteristics of *Acomys* and *Mus* cardiomyocytes.**
624 (A) Representative images of isolated cardiomyocytes from C57BL6-*Mus* and *Acomys* stained
625 with di-8-ANEPPS to visualize T-tubules. (B-D) T-tubule analysis shows significantly
626 greater T-tubule density in transverse (B) and axial directions (C) along with wider T-tubule
627 spacing (D) in *Acomys* compared to *Mus* (C57BL6; t=6.2, 12, and 4.4; F=39, 141, and 19, for
628 panels B, C, and D, respectively; *Mus* N=5, n=67; *Acomys* N=3, n=23. (E) Current traces (left)
629 current-voltage relationship (right) elicited by V_{test} -25mV (left, upper) & V_{test} +15mV (left,
630 lower) from V_{hold} -80mV. (F, left). Current-voltage curves from V_{hold} -80mV and -50 mV
631 superimposed for *Acomys* CM exhibiting $I_{Ca,T}$ (A) or no $I_{Ca,T}$. (F, center) $I_{Ca,T}$ expression was
632 heterogeneous but more *Acomys* ventricular CMs showed $I_{Ca,T}$ compared to rare occurrences
633 in *Mus*-C57BL6. (F, right) Cell capacitance was not different for *Acomys* CM with or without
634 $I_{Ca,T}$. (G) Cell capacitance was greater in *Mus*-C57BL6 compared to *Acomys* (t=2.88, F=7.9,

635 **P<0.01). (H) Maximal conductance density trended greater in *Mus*-C57BL6 compared to
636 *Acomys* (t=2.0, F=7.7, P=0.06). (I-J) Voltage-dependent activation and inactivation of $I_{Ca,L}$ was
637 significantly shifted positive for *Acomys* compared to *Mus*-C57BL6 (t=5.8 and 5.2, F=3.7 and
638 4.5, for panels I and J, respectively, ****P<0.001). (K) Representative calcium transients from
639 isolated ventricular cardiomyocytes loaded with fura2-AM, *Mus*-C57BL6 (top, red) and
640 *Acomys* (bottom, blue) paced at 1 Hz. Scale bar: 2 seconds. (K, right) Amplitude of the
641 transients (t=3.7, F=1.4, ***P = 0.0004). Velocity at which calcium enters the cytosol (upstroke
642 of the transient: t=2.1, F=1.5, *P=0.04). (τ) Calcium transient decay (t=3.6, F=1.5,
643 ***P=0.0005). (L) Representative calcium transients treated with 100 nM isoproterenol (ISO),
644 *Mus*-C57BL6 (top, red) and *Acomys* (bottom, blue), paced at 1 Hz. Scale bar: 2 seconds. (Left)
645 Before and after ISO Amplitude of the transients (t=2.8 for Mus, P=0.53, t=0.7 for Acomys,
646 **P= 0.007). (Middle) Before and after ISO Velocity at which calcium enters the cytosol (t=2.5,
647 P = 0.02). (Right) Calcium transient decay (t=3.4 for *Mus*, **P = 0.002; N=7 animals, n=37
648 cells for C57BL6-*Mus*; and N=4 animals, n=31 cells for *Acomys)*.
649
650 **Figure 4. Myocardial ischemic injury response in Acomys and Mus.**
651 (A) Representative M-mode echocardiography images of *Mus*-C57BL6) (left), *Mus*-SWR
652 (middle) and *Acomys* (right) at baseline (upper images) and day 50 after MI (lower images).
653 Delta (Δ) ejection fraction (EF) (B), Δ left ventricular end-diastolic diameter (LVEDD) (C),
654 Δ left ventricular end-systolic diameter (LVESD) (D), Δ left ventricular end-diastolic volume
655 (LVEDV) (E), and Δ left ventricular end-systolic volume (LVESV) (F) after injury, calculated
656 as difference between each time point and baseline value in the same animal (N = 16-45 *Mus*-
657 C57BL6, 10-20 *Mus*-SWR and 8-11 *Acomys*) (Values are means ± S.E.M, *P < 0.05 by Mixed
658 -effects ANOVA, compared to **Mus*-C57BL6 or #*Mus*-SWR). (G) Quantitation of heart weight
659 (HW) normalized by body weight (BW) for *Mus*-C57BL6 (N = 2-26 animals), *Mus*-SWR (N
660 = 3-11 animals) and *Acomys* (N = 2-13 animals) at baseline and various timepoints after MI

661 suggesting maintenance of HW/BW ratio in *Acomys* and progressive increase in *Mus* (Values
662 are means ± S.E.M, $P < 0.05$ by two-way ANOVA, compared to **Mus*-C57BL6 or #*Mus*-SWR).
663 (H) Quantitation of wet-dry lung weight normalized by body weight of *Mus*-C57BL6 (2-26
664 animals), *Mus*-SWR (3-11 animals) and *Acomys* (1-13 animals) at various timepoints after MI
665 suggesting maintenance of wet-dry lung weight/body weight ratio in *Acomys* and progressive
666 increase in *Mus* (Values are means ± S.E.M, *$P < 0.05$ by two-way ANOVA, compared to
667 **Mus*-C57BL6 or #*Mus*-SWR). (I) Kaplan-Meier analysis depicting mortality after MI and
668 showing significantly lower mortality in *Acomys* compared with *Mus* (Gehan-Bareslow-
669 Willcoxon test, $P<0.05$). (J) Representative cardiac magnetic resonance (CMR) images
670 showing comparably medium-sized infarct area in both species at three days post MI (arrows
671 show the boundaries of late gadolinium enhancement/injury). The progression of infarct area
672 was significantly slower in *Acomys* compared to *Mus* at 14 days after MI (N= 9-10 animals per
673 group, t=3.28, *$P< 0.05$ by paired T-test).
674
675 **Figure 5. *Acomys* exhibit cardiac tissue preservation in response to myocardial infarction.**
676 (A) Representative images of Masson trichrome stained long-axis left ventricular cavity
677 sections of *Mus* (C57BL6 and SWR) and *Acomys* 50 days post-MI (scale bar = 500 μm).
678 Quantification of the infarct size, corresponding to the ratio between infarcted length and left
679 ventricular length showing significantly smaller scar in *Acomys* compared to *Mus* strains (N=
680 17 *Mus*-C57BL6, 11 *Mus*-SWR, and 5 *Acomys,* values are means ± S.E.M, *$P< 0.05$ by one-
681 way ANOVA and Tukey multiple comparison test). (B) Representative images of picrosirius
682 red stained scar center 50 days after MI across species showing alignment of collagen fibers in
683 *Acomys* compared to *Mus* species. Both *Mus* strains show highly compressed, parallel collagen
684 fibers, while *Acomys* fibers show more porosity between fibers and a wavy organization.
685 Quantification of minimum and maximum scar thickness showing that *Acomys* has on average
686 a comparatively thicker scar compared to *Mus* strains (N= 3 animal/group, values are means ±

687 S.E.M, **P< 0.01 by one-way ANOVA and Tukey multiple comparison test). There was no
688 statistically significant difference in maximum scar thickness. (C) DAPI images were obtained
689 in the center of the scar and demonstrate higher cellularity in *Acomys* compared to *Mus* strains
690 (scale bar = 100 μm in upper panel and 10 μm in lower panel, yellow boxes indicating insets).
691 Quantitative analysis showed higher density of nuclei and scar percentage cellularity in *Acomys*
692 vs. *Mus* strains (N= 3 animal/group, values are means ± S.E.M, **P< 0.01 by one-way ANOVA
693 and Tukey multiple comparison test).
694
695 **Figure 6. Cardiac scar tissue exhibits limited expansion in *Acomys***
696 (A) Representative images of Masson trichrome stained long-axis left ventricular cavity
697 sections of *Mus* (C57BL6 and SWR) and *Acomys* in uninjured and MI animals at 7-, 17- and
698 50-days post-MI showing the progression of scar across species (scale bar = 500 μm). The
699 lower panels represent the boxed areas and show the composition of the scar center at each
700 stage. (B and C) Quantification of the infarct size, corresponding to the ratio between infarcted
701 length and left ventricular length showing significantly smaller scar in *Acomys* compared to
702 *Mus* strains (N= 17 *Mus*-C57BL6, 11 *Mus*-SWR, and 5 *Acomys,* values are means ± S.E.M,
703 *P< 0.05 by one-way ANOVA and Tukey multiple comparison test). (D) Delta change in scar
704 size among species showing the reduced delta in *Acomys* compared to *Mus*.
705
706 **Figure 7. Enhanced angiogenesis and vessel maturation in the infarct region following MI**
707 **in *Acomys* compared to *Mus* strains.**
708 (A) Representative images of isolectin staining (red) defining endothelial cells in the peri-
709 infarct region and the center of the scar at the mid left ventricular cavity level of *Mus* (C57BL6
710 and SWR) and *Acomys* 50 days post-MI (scale bar = 25 μm). Quantification of capillary density
711 showing significantly higher capillary density in *Acomys* compared to *Mus*-C57BL6 in the peri-
712 infarct region and to both *Mus* strains in the center of the scar (N= 4 *Mus*-C57BL6, 4 *Mus*-

713 SWR, and 5 *Acomys,* values are means ± S.E.M, *P< 0.05 by one-way ANOVA and Tukey
714 multiple comparison test). (B) Representative images of isolectin (red) and EdU staining
715 (white) marking proliferating endothelial cells in the peri-infarct region and the center of the
716 scar at the mid left ventricular cavity level of *Mus* (C57BL6 and SWR) and *Acomys* 50 days
717 post-MI (scale bar = 25 μm). Quantification of isolectin+/EdU+ cells showing significantly
718 higher endothelial cell proliferation in *Acomys* compared to the two *Mus* strains in both peri-
719 infarct and scar center areas (N= 4 *Mus*-C57BL6, 4 *Mus*-SWR, and 5 *Acomys,* values are means
720 ± S.E.M, F = 28.4, *P< 0.05 by one-way ANOVA and Tukey multiple comparison test). (C)
721 Representative images of smooth muscle actin staining (red) in the scar center region showing
722 higher prevalence of medium sized blood vessels in *Acomys* compared to *Mus* strains.
723 Autofluorescence (green) was used to identify the infarct boundary (scale bar = 25 μm).

724

Figure 1

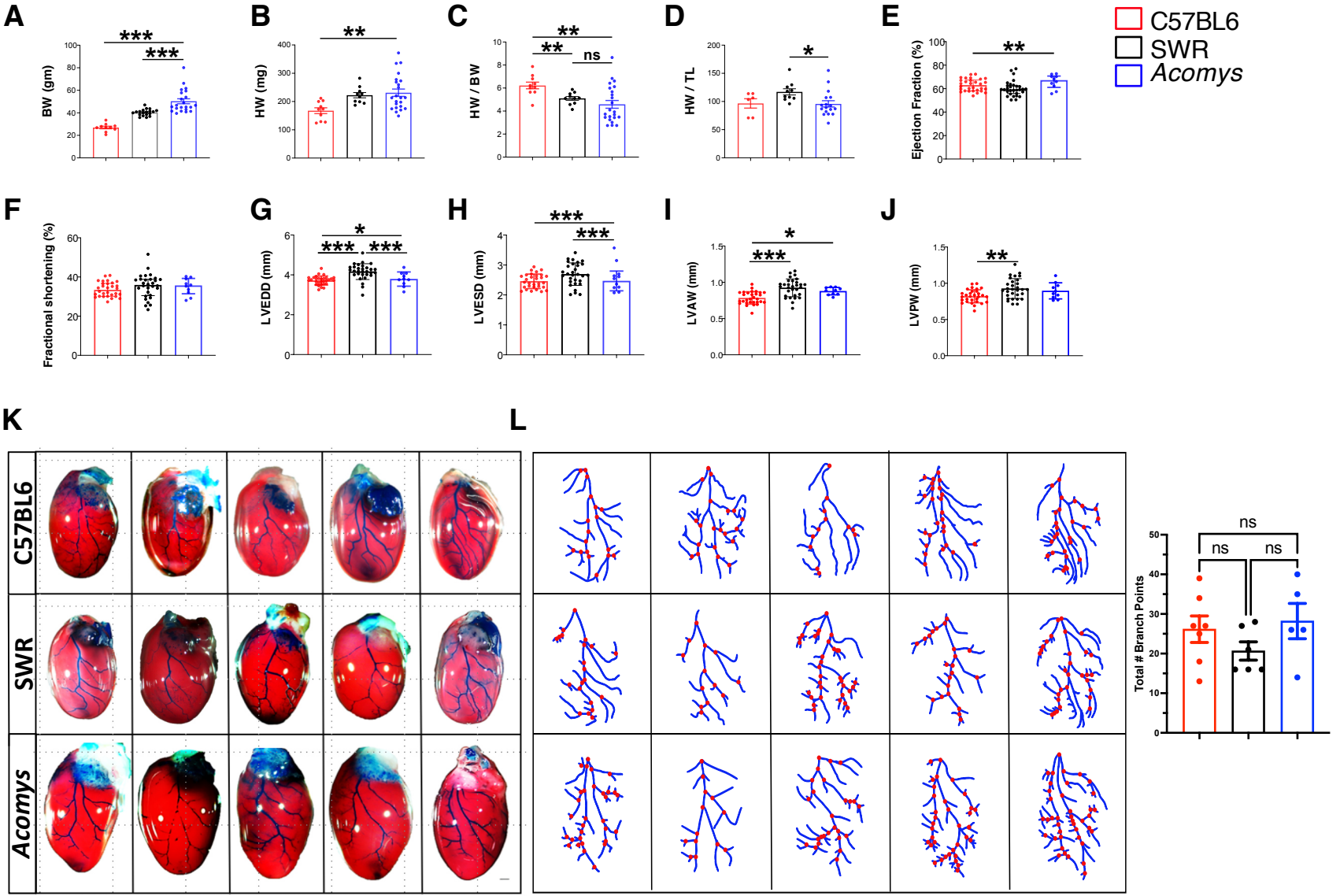
A
BW (gm)
B
HW (mg)
C
HW / BW
D
HW / TL
E
Ejection Fraction (%)
C57BL6
SWR
Acomys
F
Fractional shortening (%)
G
LVEDD (mm)
H
LVESD (mm)
I
LVAW (mm)
J
LVPW (mm)
K
C57BL6
SWR
Acomys
L
Total # Branch Points
ns

Figure 2

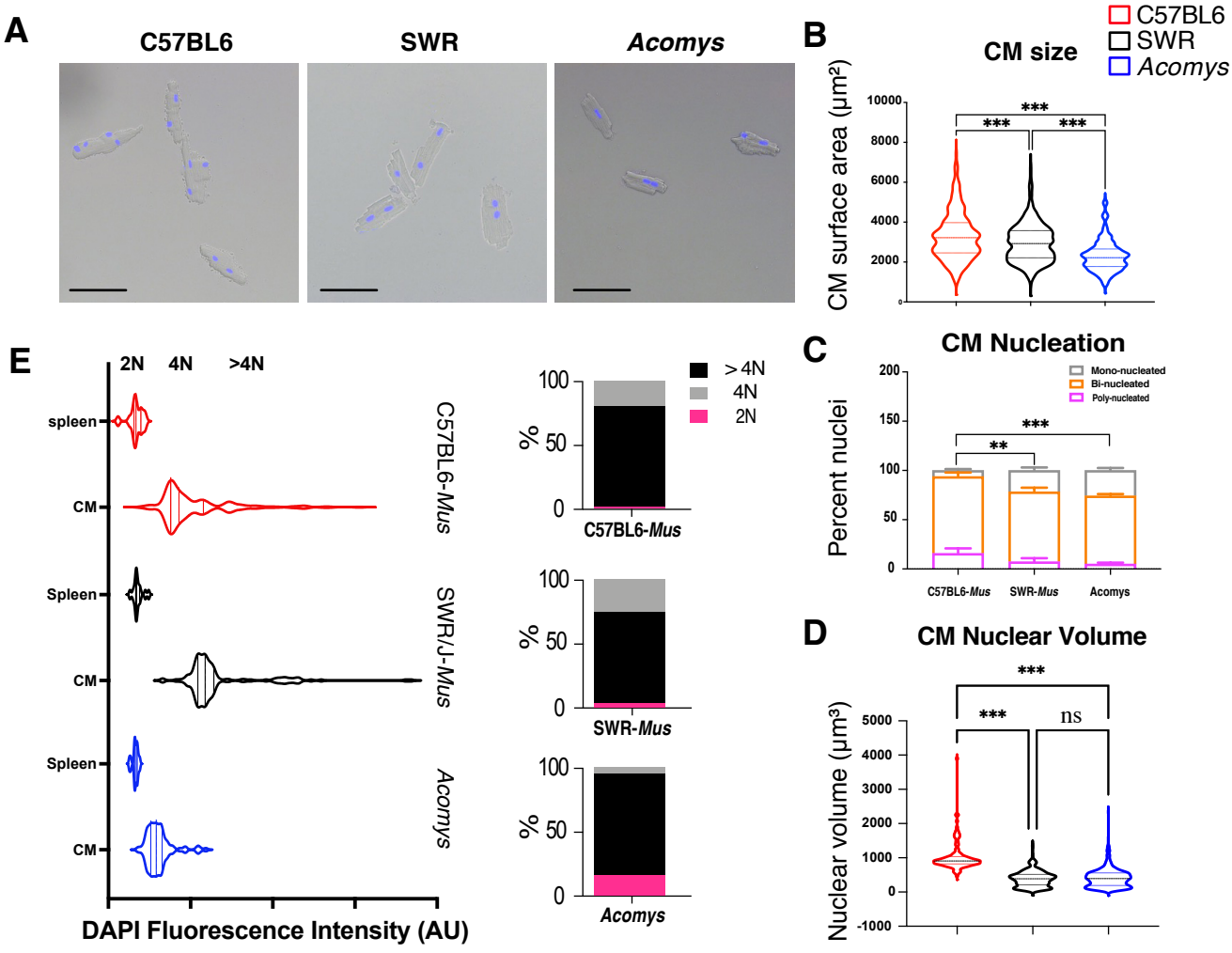
A
C57BL6
SWR
Acomys
B
CM size
C57BL6
SWR
Acomys
CM surface area (µm²)
10000
8000
6000
4000
2000
0
***
***
***
C
CM Nucleation
Mono-nucleated
Bi-nucleated
Poly-nucleated
Percent nuclei
200
150
100
50
0
***
**
C57BL6-Mus
SWR-Mus
Acomys
D
CM Nuclear Volume
Nuclear volume (µm³)
5000
4000
3000
2000
1000
0
-1000
***
***
ns
E
2N
4N
>4N
spleen
CM
Spleen
CM
Spleen
CM
C57BL6-Mus
SWR/J-Mus
Acomys
DAPI Fluorescence Intensity (AU)
> 4N
4N
2N
%
100
50
0
C57BL6-Mus
SWR-Mus
Acomys

Figure 3

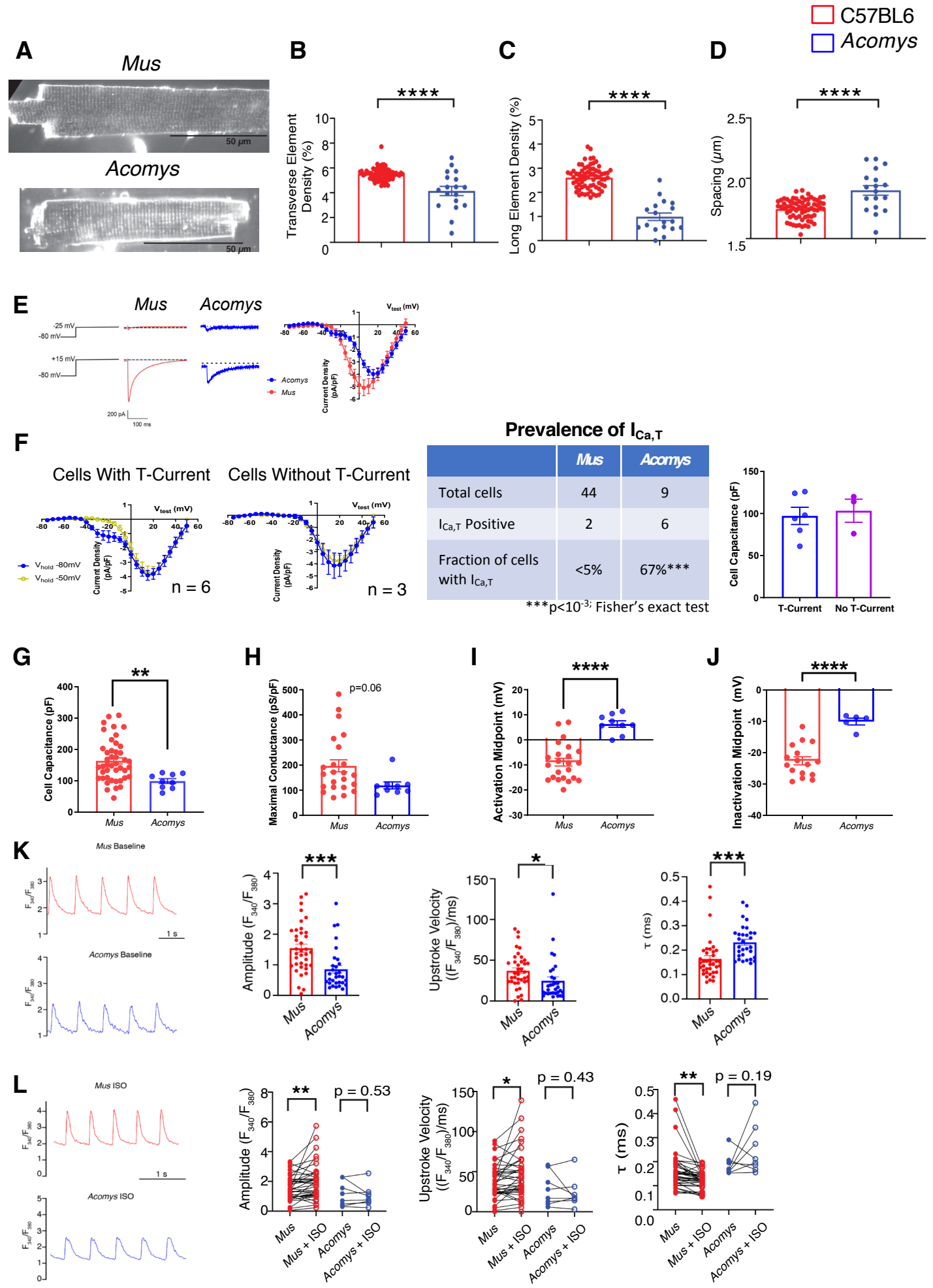
C57BL6
Acomys
A
Mus
50 μm
Acomys
50 μm
B
Transverse Element Density (%)
****
C
Long Element Density (%)
****
D
Spacing (μm)
****
E
Mus
Acomys
-25 mV
-80 mV
+15 mV
-80 mV
200 pA
100 ms
Acomys
Mus
Current Density (pA/pF)
V_test (mV)
F
Cells With T-Current
Cells Without T-Current
V_test (mV)
Current Density (pA/pF)
V_hold -80mV
V_hold -50mV
n = 6
n = 3
Prevalence of I_Ca,T
Mus
Acomys
Total cells 44 9
I_Ca,T Positive 2 6
Fraction of cells with I_Ca,T <5% 67%***
***p<10^-3; Fisher's exact test
Cell Capacitance (pF)
T-Current
No T-Current
G
Cell Capacitance (pF)
**
Mus
Acomys
H
Maximal Conductance (pS/pF)
p=0.06
Mus
Acomys
I
Activation Midpoint (mV)
****
Mus
Acomys
J
Inactivation Midpoint (mV)
****
Mus
Acomys
K
Mus Baseline
Acomys Baseline
1 s
Amplitude (F340/F380)
***
Upstroke Velocity ((F340/F380)/ms)
*
τ (ms)
***
Mus
Acomys
L
Mus ISO
Acomys ISO
1 s
Amplitude (F340/F380)
**
p = 0.53
Upstroke Velocity ((F340/F380)/ms)
*
p = 0.43
τ (ms)
**
p = 0.19
Mus
Mus + ISO
Acomys
Acomys + ISO

Figure 4

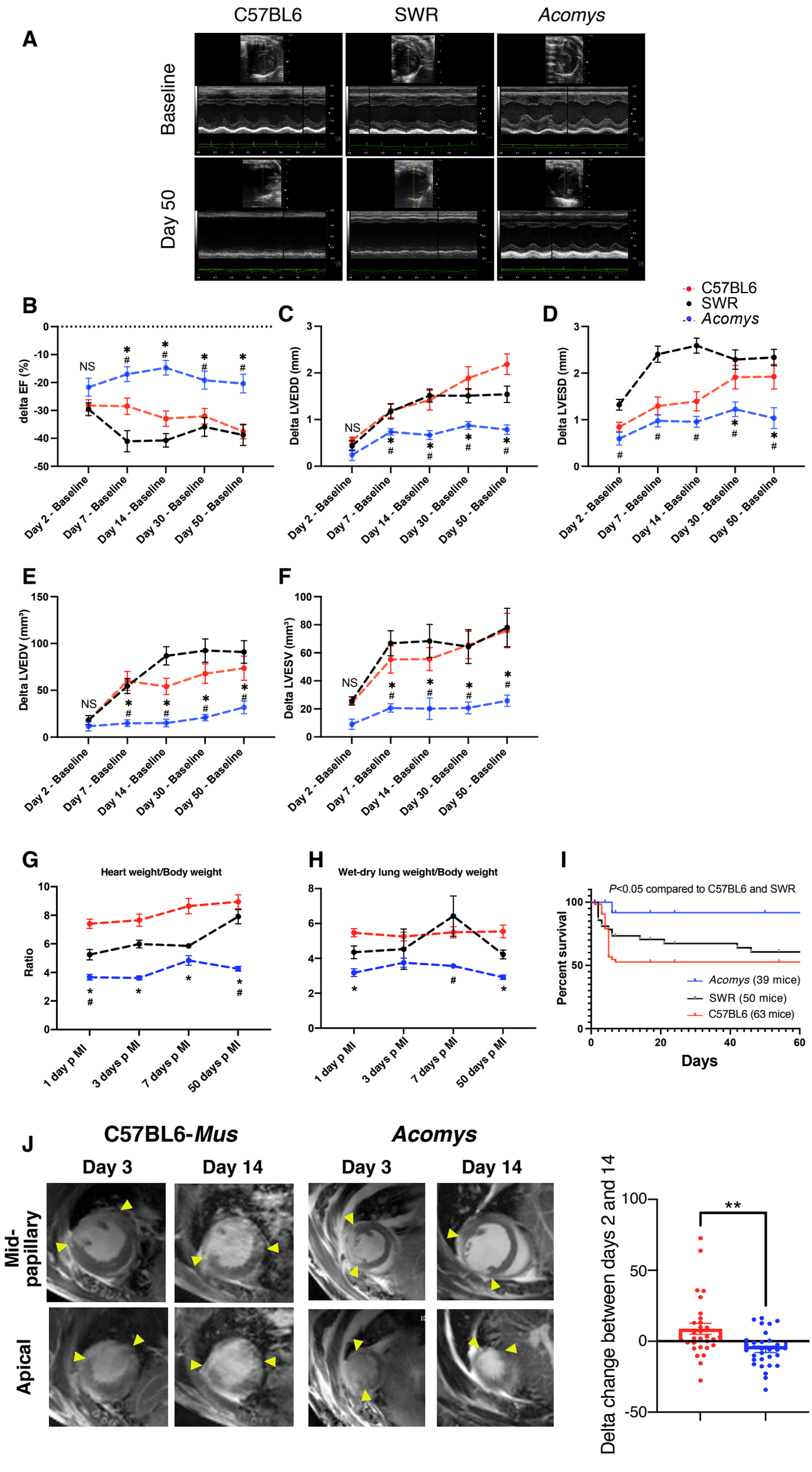
A
C57BL6
SWR
Acomys
Baseline
Day 50
B
delta EF (%)
NS
C
Delta LVEDD (mm)
D
Delta LVESD (mm)
C57BL6
SWR
Acomys
Day 2 - Baseline
Day 7 - Baseline
Day 14 - Baseline
Day 30 - Baseline
Day 50 - Baseline
E
Delta LVEDV (mm³)
F
Delta LVESV (mm³)
G
Heart weight/Body weight
Ratio
H
Wet-dry lung weight/Body weight
1 day p MI
3 days p MI
7 days p MI
50 days p MI
I
P<0.05 compared to C57BL6 and SWR
Percent survival
Acomys (39 mice)
SWR (50 mice)
C57BL6 (63 mice)
Days
J
C57BL6-Mus
Acomys
Day 3
Day 14
Mid-papillary
Apical
Delta change between days 2 and 14
**

Figure 5

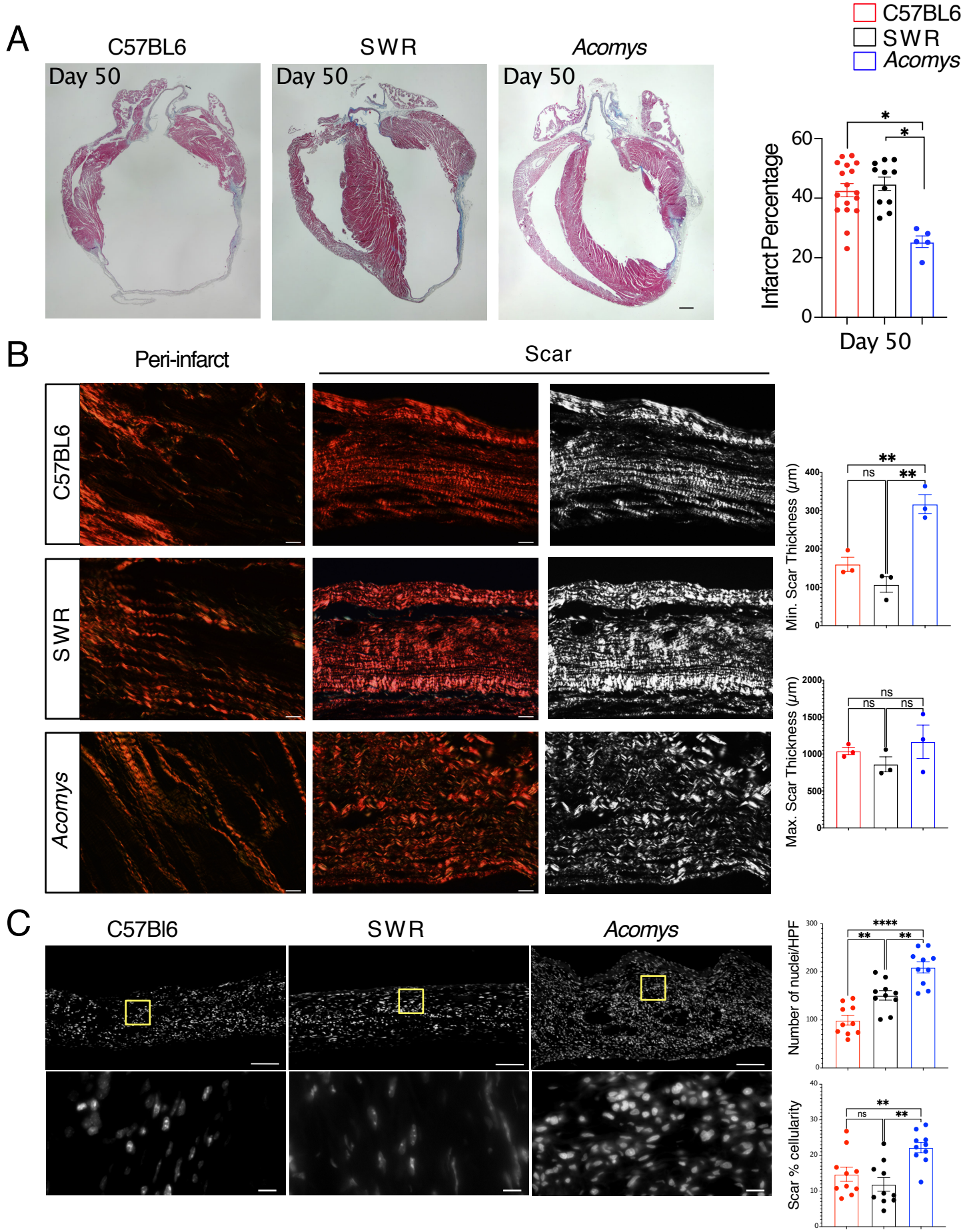
C57BL6
SWR
Acomys
A
C57BL6
SWR
Acomys
Day 50
Day 50
Day 50
Infarct Percentage
60
40
20
0
*
*
Day 50
B
Peri-infarct
Scar
C57BL6
SWR
Acomys
Min. Scar Thickness (μm)
400
300
200
100
0
**
ns
**
Max. Scar Thickness (μm)
2000
1500
1000
500
0
ns
ns
ns
C
C57Bl6
SWR
Acomys
Number of nuclei/HPF
300
200
100
0
****
**
**
Scar % cellularity
40
30
20
10
0
**
ns
**

Figure 6

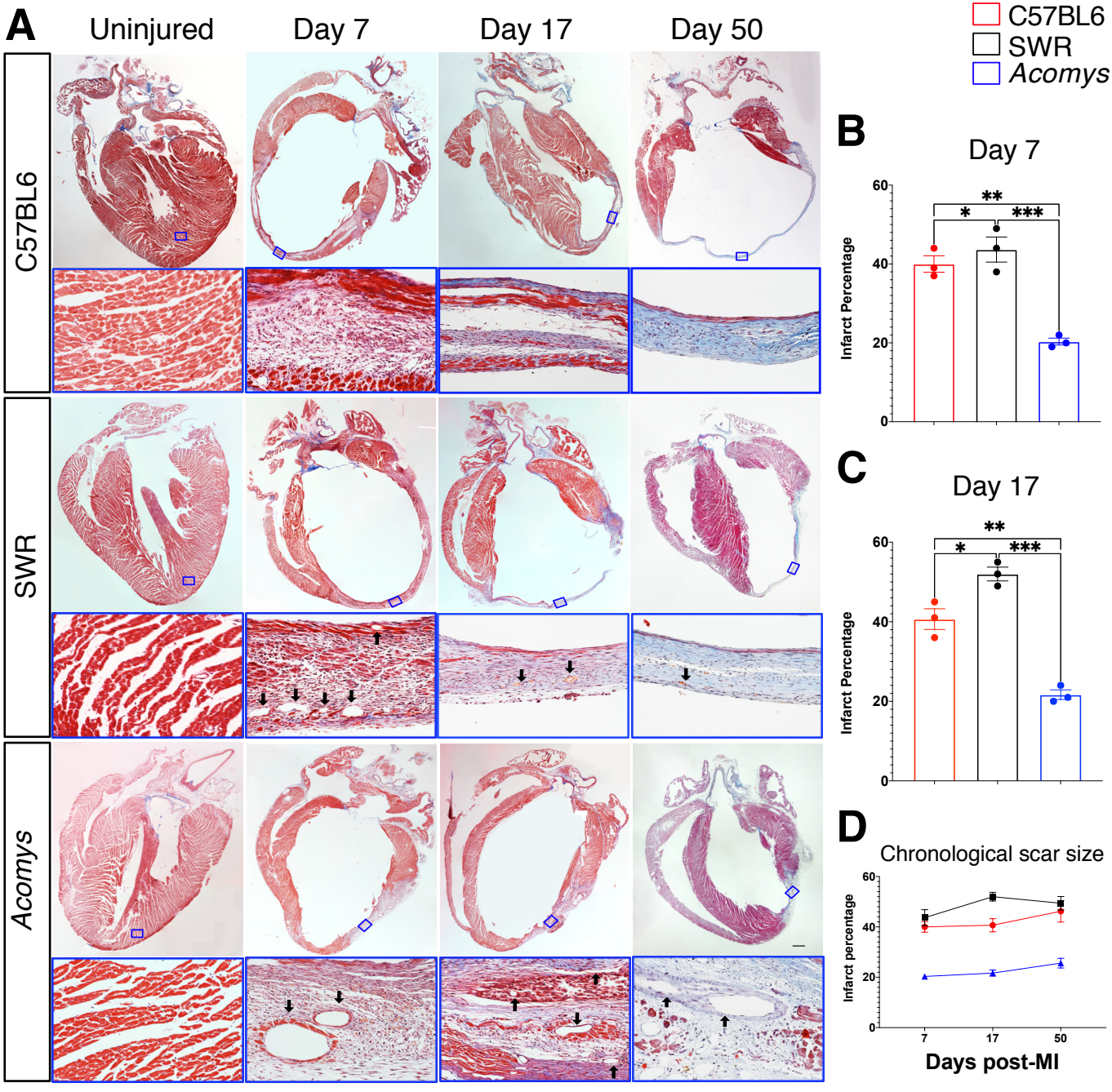
A
Uninjured
Day 7
Day 17
Day 50
C57BL6
SWR
Acomys
C57BL6
SWR
Acomys
B
Day 7
Infarct Percentage
60
40
20
0
**
*
***
C
Day 17
Infarct Percentage
60
40
20
0
**
*
***
D
Chronological scar size
Infarct percentage
60
40
20
0
7
17
50
Days post-MI

Figure 7

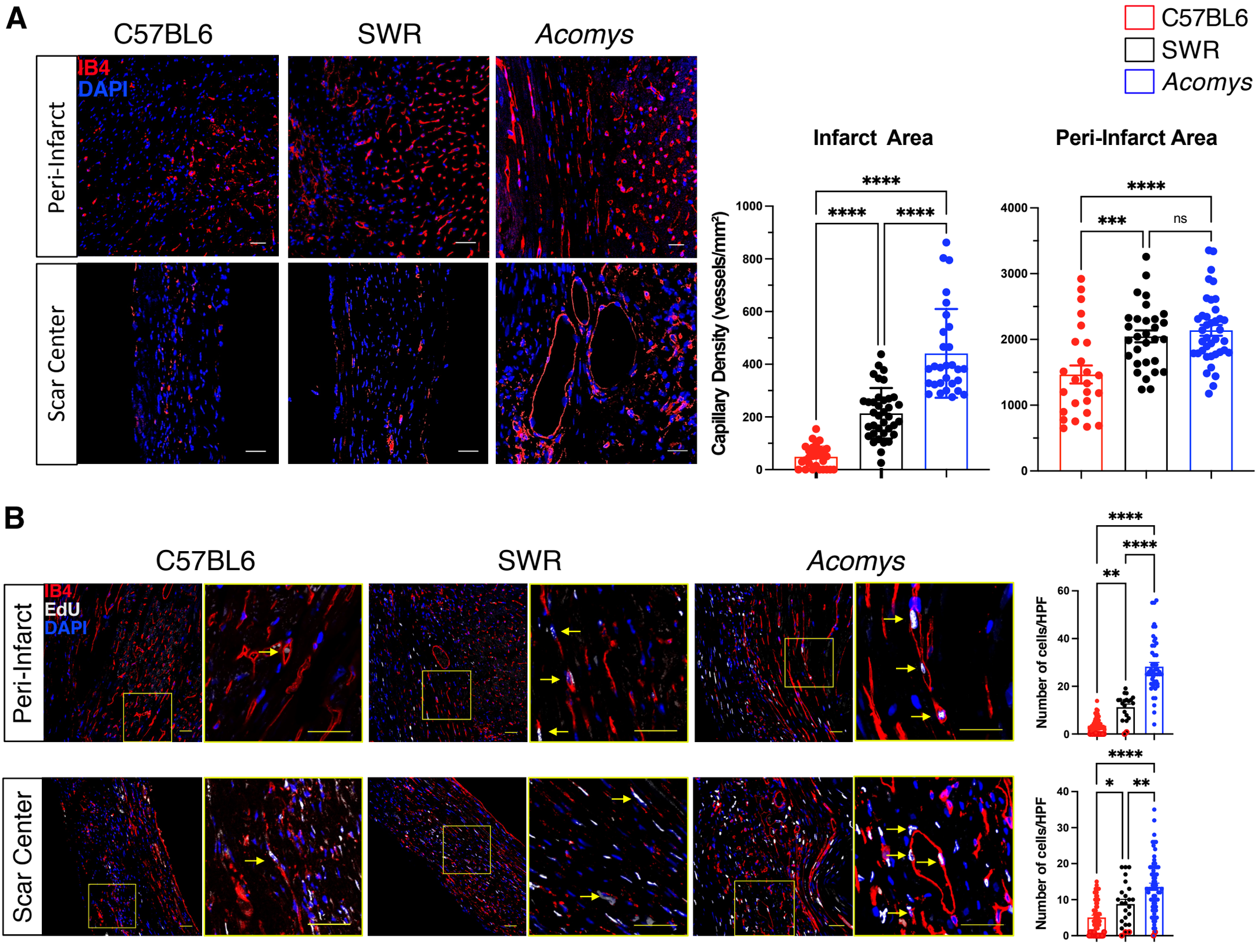
A
C57BL6
SWR
Acomys
Peri-Infarct
Scar Center
IB4
DAPI
Infarct Area
Peri-Infarct Area
Capillary Density (vessels/mm²)
****
***
ns
B
EdU
Number of cells/HPF
**
*

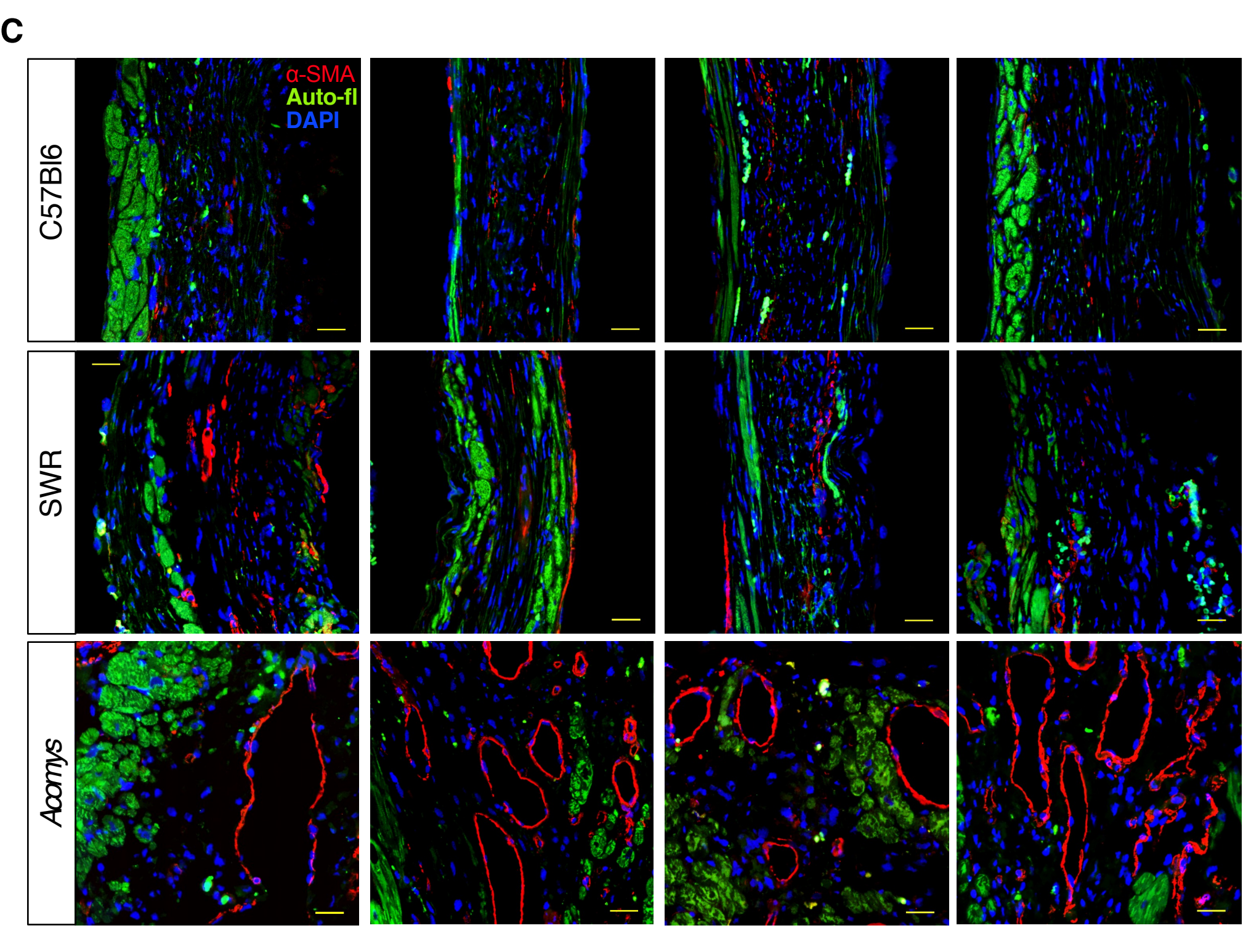
C
α-SMA
Auto-fl
DAPI
C57Bl6
SWR
Acomys